https://doi.org/10.5194/wes-2026-81
Preprint. Discussion started: 8 May 2026

eawe european academy of wind energy
Open Access WIND ENERGY SCIENCE DISCUSSIONS

AI enhanced fault indicators vs. classical bearing monitoring - example results of bearing tests and transferability to wind turbines

Matthias Stammler[1, 3], Faras Jamil[2], Xinrun Liu[1], Jens Jo Matthys[2], Nikhil Sudhakaran[1], Cédric Peeters[2,4], Asger Bech Abrahamsen[1], and Jan Helsen[2,4]

[1]Technical University of Denmark, Frederiksborgvej 399, 4000 Roskilde, Denmark
[2]OWI-Lab, Vrije Universiteit Brussel, Pleinlaan 2, 1050 Brussel, Belgium
[3]Fraunhofer Institute for Wind Energy Systems, Large Bearing Laboratory, Am Schleusengraben 22, 21029 Hamburg, Germany
[4]FlandersMake@VUB, Belgium

Correspondence: Matthias Stammler (masta@dtu.dk)

Abstract.

Condition monitoring of drive trains is indispensable in the operation of wind turbines. Early knowledge of faults allows for maintenance planning and in-situ counter-measures and thus reduces operational costs. Current commercial methods include significant human supervision and interpretation of measurement data. Larger fleets of assets raise the need for enhanced methods that require reduced supervision and less manual interaction. The present work verifies two ways of using artificial intelligence that fulfill this requirement. These are normal-behaviour models and high-level indicators. The verification includes test data analysis of small-scale bearing tests of Ø100 mm thrust bearings and considerations of transfer to wind turbines. In bearing tests, enhanced monitoring gives comparable or significantly earlier warnings than classical monitoring. In three of five performed tests, the warning thresholds were passed at comparable times, in two, the warnings were significantly earlier and clearer with the enhanced monitoring. As classical monitoring benefits most from the simplified test environment, it is reasonable to assume an even more pronounced advantage for enhanced monitoring in more complex machines like wind turbines.

1 Introduction

1.1 Condition monitoring in drive trains

Wind energy is a central pillar of the supply of renewable energy (Backwell et al., 2025). From modest beginnings in the 1970s and 1980s, commercial wind turbines have developed into the biggest rotating machines humans have built (Memija, 2025). Wind turbines face environmental conditions and unsteady winds for design lifetimes of 20 years and more (Burton et al., 2011). Recent service contracts extend up to 35 years (Vestas, 2023). Dynamic loads and speed changes challenge the rolling bearings most commonly used in the drive trains and can cause various different faults (Hart et al., 2023; Haus et al., 2025). Some of them cause turbine downtimes and high repair costs, especially if parts of or the entire rotor have to be removed from

https://doi.org/10.5194/wes-2026-81
Preprint. Discussion started: 8 May 2026

eawe european academy of wind energy
Open Access WIND ENERGY SCIENCE DISCUSSIONS

the nacelle for a bearing exchange. Carroll et al. (2016) give average costs of €230,000 for major gearbox repairs for the 2-4 MW turbines, and it is reasonable to assume these costs have not gone down with larger turbines sizes.

Given the costs for downtime and the necessary logistical planning for major repairs, it is but evident that continuous health monitoring of bearings in wind turbines reduces operations and maintenance costs, because it facilitates more efficient works. IEC 61400-1 foresees reduced safety factors for monitored bearings (IEC, 2019). The use of vibrational sensors and analysis of their data is one of the common condition monitoring approaches. Broad-band monitoring is outlined in ISO28016-21 (ISO, 2025), but frequency-band monitoring is commonly used for rolling bearings. Kestel et al. (2025) give a comprehensive overview of the state of the art in this field.

Condition monitoring and subsequent data analysis of bearings should achieve three objectives:

- Detect bearing fault as early as possible
- Monitor the development of the bearing's condition to plan repair
- Inform about the remaining useful life of the bearing

To the knowledge of the authors, the last two objectives are not commonly achieved with state-of-the-art methods. State-of-the-art methods further require significant human supervision and interpretation of data, especially when monitoring large fleets of complex machines like wind turbines in wind farms.

The present work aims to compare two different approaches in terms of detection and development monitoring. On the one side, it uses classical condition monitoring techniques, i.e. static algorithms for postprocessing of vibrational data, on the other side, these algorithms are extended by artificial intelligence to form a high-level health indicator trend. The main purpose of this high-level indicator is to fuse many incoming signals into one, easy to interpret trend per machine.

1.2 Classical condition monitoring

Classical condition monitoring (CM) in the context of this work is a physics-based approach that relies on vibration measurements and signal processing with static algorithms, see also ISO 13373-2 and ISO 13373-3 ISO (2016, 2015). The main objective is to identify changes in machine behaviour that indicate the onset and development of faults in one or more components by analysing the signals in the time and frequency domains.

In practice, vibration signals are first processed in the time domain to evaluate overall amplitude levels and statistical indicators, such as root mean square (RMS) and mean value. Subsequently, the raw signals are transformed into the frequency domain to further reveal fault-related signatures. The most widely used frequency-domain techniques include:

- Fast Fourier Transform (FFT), see Cooley and Tukey (1965), which transforms time-domain data into the spectral domain to expose dominant frequencies and harmonics
- Short-Time Fourier Transform (STFT), see Allen and Rabiner (1977), which extends the FFT by applying a moving time window to obtain a time–frequency representation suitable for analysing non-stationary vibration signals

https://doi.org/10.5194/wes-2026-81
Preprint. Discussion started: 8 May 2026

eawe european academy of wind energy
Open Access WIND ENERGY SCIENCE DISCUSSIONS

- Envelope analysis (Poularikas, 1998), used for demodulating high-frequency resonance to detect bearing faults
- Spectral kurtosis, see Antoni (2006), which isolates frequency bands containing impulsive or non-stationary behavior.

These methods rely on predefined characteristic frequencies of the drivetrain, such as the shaft rotational frequency, gear-mesh frequencies, and bearing defect frequencies such as ball passing frequency outer(BPFO) and inner race (BPFI), respectively, ball spin frequency (BSF) (SKF, 2011)). Note the terms for characteristical frequencies commonly refer to 'ball' but are also also applicable for rollers and other rolling bodies.

Hart et al. (2023) analysed large-scale field data on main-bearing failures, demonstrating the widespread application of classical condition monitoring in wind turbine drive trains and its importance for maintenance planning. For a comprehensive methodological background, Randall and Antoni (2011) provide a tutorial summarizing classical signal-processing techniques such as FFT, STFT, and envelope analysis, and discuss best practices for condition monitoring of rolling-element bearings.

1.3 Artificial-intelligence enhanced condition monitoring

Condition monitoring indicators track distinct signal patterns to diagnose different fault mechanisms. They require continuous monitoring to assess the condition of mechanical components. Early fault detection becomes increasingly challenging when experts manually monitor multiple indicators of different scales, and subtle changes in a trend can easily be overlooked. Furthermore, it is essential to track multiple indicators because different indicators are sensitive to different fault types. These limitations challenge traditional condition monitoring for large fleets of complex machines, such as wind turbines. Artificial intelligence (AI) techniques can simplify and automate the condition monitoring process (Chesterman et al., 2023). In the context of this work, such AI techniques are in two fields:

1. Combination of individual indicators to high-level indicators
2. Use of normal behavior models to determine faults without knowing their signal characteristics

Despite the wide use of vibration analysis for condition monitoring, and its potential in practical application, the fusion of multiple condition indicators into a single interpretable metric remains relatively underexplored in the literature. Existing work includes a regression-based normal behavior modeling approach that labels individual condition indicators as healthy or faulty, which are then combined to derive a high-level health indicator (Jamil et al., 2025). A deep learning–based normal behaviour method fusing time-domain statistical (Jamil et al., 2023a) and frequency-domain indicators (Jamil et al., 2023b) has been validated using wind farm data, demonstrating real-time industrial applicability for wind turbine drivetrain condition monitoring under varying operational and environmental conditions.

Obtaining sufficient faulty data to train fault detection models remains a challenge, as machines typically operate under healthy conditions. Transfer learning can help mitigate this issue by employing the data from similar machines (Jamil et al., 2022). However, for newly installed machines with only healthy data available, a more practical solution is to develop normal behaviour models, which require only healthy operational data for training. These models learn the inherent characteristics of healthy machine operation and identify faults by detecting deviations from the learned normal behavior (Jamil et al., 2025).

https://doi.org/10.5194/wes-2026-81
Preprint. Discussion started: 8 May 2026

eawe european academy of wind energy
Open Access WIND ENERGY SCIENCE DISCUSSIONS

Statistical normal behaviour models, such as principal component analysis (PCA) (Pozo et al., 2018) and auto-regressive integrated moving averages (ARIMA) (Chesterman et al., 2021), are typically applied to SCADA data for wind turbine health monitoring. These statistical methods are simple and easy to interpret; however, they lack the ability to capture complex nonlinear relationships in the data.

Machine learning–based approaches, such as one-class classification (OCC) (Khan and Madden, 2010), have also been applied, where the one-class support vector machine (OCSVM) (Laouti et al., 2011) is trained on healthy data to detect wind turbine blade pitch position faults and blade icing. Tree-based normal behaviour methods, such as the Isolation Forest, are used for gearbox fault detection (Du et al., 2022).

A regression-based method trained solely on vibration-based condition monitoring indicators, without using operating condition data, has been used to detect gearbox bearing faults (Rao et al., 2025). Also SCADA data collected during healthy operation has been used to train autoencoders for drivetrain health monitoring (Chen et al., 2021; Zhao et al., 2018). Table 1 summarises normal behaviour approaches from the literature.

Table 1. Summary of existing normal behaviour condition monitoring approaches.

Category & References	Methods	Input	Fault Detection Application	Characteristics
Statistical models (Chesterman et al., 2021; Pozo et al., 2018)	PCA, ARIMA	SCADA	Generator bearings; pitch and torque actuators	Simple and interpretable, limited capability in modelling nonlinear relationships.
One-class anomaly (**?**)	OCSVM, DSVDD	SCADA	Pitch actuators, speed sensor, gearbox	Highly generalizable yet critically dependent on feature engineering.
Tree-based methods (Du et al., 2022)	Isolation Forest	Vibration	Gearbox	Unsupervised anomaly detection via randomised tree ensemble with limited interpretability.
Transfer learning (Jamil et al., 2022)	Deep boosted transfer learning	Vibration, SCADA	Gearbox	Minimises faulty data requirement and prevents negative transfer, but depends on machine similarity.
Vibration regression (Rao et al., 2025)	Regression	Vibration	Gearbox bearing	Operating condition invariant; requires model retraining post-major maintenance
DL-based SCADA (Chen et al., 2021; Zhao et al., 2018)	Autoencoders	SCADA	Gearbox, generator, pitch and yaw	Capture nonlinear operational behaviour; require continuous SCADA access.
Indicator fusion (Jamil et al., 2025, 2023a, b)	Autoencoder and regression	Vibration, SCADA	Drivetrain	Combine multiple indicators into a single health metric.

https://doi.org/10.5194/wes-2026-81
Preprint. Discussion started: 8 May 2026

eawe european academy of wind energy
Open Access WIND ENERGY SCIENCE DISCUSSIONS

1.4 Summary

Condition Monitoring of rolling bearings is state of the art in the wind industry. With growing fleets and the need to reduce operation costs, automation becomes more attractive. AI methods can condense hundreds of signals to high-level health indicators and thus eliminate the need for human supervision of individual signals.

A reduction of signals bears the risk of information loss, and the research question addressed in this work is thus:

- Can a combination of normal behaviour model and high-level health indicator compete with classical condition monitoring in early fault detection?

To this end, this work uses vibrational data from five bearing tests. The remainder of this work is divided as follows: Section 2 describes the test rig, test program, bearings, and data processing methods. The results are then presented in Section 3. The discussion and conclusions in Section 4 summarize the work and give an outlook on future activities.

2 Methods

2.1 Bearing test and monitoring

Testing was conducted on 81212-TV thrust bearings manufactured by Schaeffler (2024). Table 2 lists their properties. Before mounting on the test rig, the bearings were cleaned with ethanol, wiped dry, and lubricated with Mobil SHC Gear 320 WT oil. This wind turbine gearbox oil was also used in the tests.

Table 2. Dimensions and properties of the 81212 axial thrust roller bearing. Except for the rolling element dimensions and the number of rollers, all data were obtained from Schaeffler (2024). The rolling element dimensions and roller count were determined by direct measurement.

Property	Symbol	Value	Unit
Bore diameter	d_i	60	mm
Outer diameter	d_o	95	mm
Width	B	26	mm
Number of rollers	z	19	–
Rolling element diameter	D_W	11	mm
Rolling element length	L_W	11	mm
Effective rolling element length	L_we	9	mm
Static load capacity	C_0	480000	N
Dynamic load capacity	C_1	173000	N

The test rig used for this purpose was an FE8 test rig manufactured by Christoph Assmann Engineering & Industrial Services and is illustrated in Figure 1.

https://doi.org/10.5194/wes-2026-81
Preprint. Discussion started: 8 May 2026

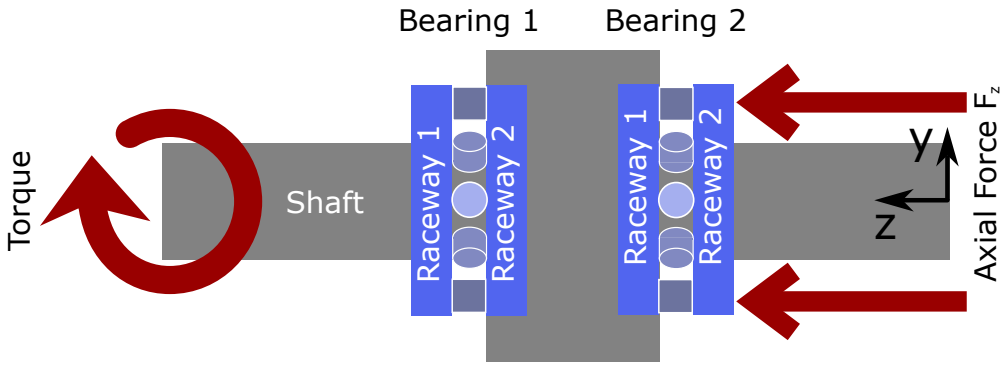

Figure 1. Layout of the FE8 shaft and bearings with their designation and the direction of torque and force

Table 3 lists the test conditions of the five test labelled T1-T5. Tests were conducted at a rotation speed of 250 rpm and with an axial load F_z = 85 kN (axial load depicted in Figure 1) except for Test T2 where the testing was conducted with an axial load F_z = 95 kN. Two bearings are tested simultaneously on the test rig. The test rig is equipped with heating elements and PT-100 temperature sensors to control and measure bearing temperature and a torque sensor to determine the torque transmitted to the bearings.

Table 3. Overview of the bearing test conditions.

Test ID	**Force**	**Rotation speed**	**Temperature**	**Contact stress**	**Oil used**
	F_z (kN)	ω (rpm)	T (°C)	σ_{Hertz} (MPa)	
T1, T3–T5	85	250	100	1800	Mobil SHC Gear 320 WT
T2	95	250	100	1900	Mobil SHC Gear 320 WT

The test rig is equipped with an accelerometer Acida AC101.51. The rig monitors the full-bandwidth acceleration amplitude. During a run-in period of approximately 12-24 hours the acceleration amplitude is observed to decrease significantly, usually by roughly 1.2 g of acceleration. The stop criterion of the bearing test is set to be 1 g higher than the acceleration amplitude after run-in. This criterion was defined after previous tests to ensure the occurrence of visible damages after test stop. Figure 2 shows low-resolution data of test T3 as referred to in later Table 5. The acceleration in purple starts at a level close to 2 g and drops after the running-in to an level below 1 g. The signals stored by the test rig controller are mean values for 2 min intervals. The other signals shown in Figure 2 are axial force, constant at 85 kN (with the exception of T2, where it is kept constant at 95 kN), speed, constant at 250 rpm, temperature (constant at appr. 100°C), and torque. The torque shows a decline during the running-in as well.

https://doi.org/10.5194/wes-2026-81
Preprint. Discussion started: 8 May 2026

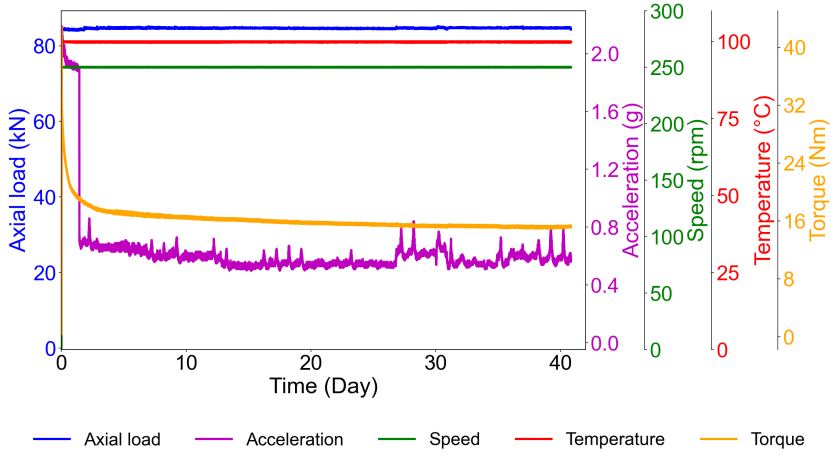

Figure 2. Monitoring of test condition as recorded with 2 minute resolution by the FE8 contoller during test T3 in Table 5

In commercially operating wind turbines, operators do not always have the required sensors which give the data for making decisions. Similarly, the control computer of the FE8 rig records low-resolution mean values in a log file, but it does not allow direct access to any external analysis of the acceleration signal, such as the Fourier transform.

To provide more data for the condition monitoring, an external accelerometer, a 356A03 piezoelectric triaxial accelerometer from PCB was installed on the housing of the test rig. For tests T1, T2 and T3 as referred to in later Table 5, data was collected from this accelerometer using a Simcenter SCADA lab system from Siemens Digital Industry Software. Tests T4 and T5 used a custom-built condition monitoring system from VUB.

The VUB system features a modular architecture that enables easy replacement of acquisition cards and edge-processing modules.

The base layer of the system provides power either through Power-over-Ethernet (PoE) or a DC supply. It includes extensive filtering circuitry that generates multiple low-noise power rails required by the sensitive acquisition subsystems. The base layer also hosts the interchangeable processing module.

For the experiments described in this work, a heterogeneous IMX8-based System-on-Module (SoM) serves as the processing unit. Its architecture allows some cores to handle real-time data acquisition while others perform system control and measurement data processing. These processing capabilities enable the system to compute high-level health indicators directly at the edge, significantly reducing the need to transmit large volumes of raw data to a central server.

An IEPE-compatible acquisition card is connected to the base layer via a PCIe interface to read data from the external accelerometer. This card includes additional signal conditioning circuitry designed to capture the smallest variations in the accelerometer signal.

https://doi.org/10.5194/wes-2026-81
Preprint. Discussion started: 8 May 2026

eawe european academy of wind energy
Open Access WIND ENERGY SCIENCE DISCUSSIONS

2.2 Classical data postprocessing

Classical monitoring commonly focuses on tracking the development of characteristic fault frequencies in the envelope spectrum. The time-domain acceleration signal $x(t)$ is first converted into an analytic signal as described by Gabor (1946),

$$x_{\mathrm{a}}(t) = x(t) + j\,\mathcal{H}\{x(t)\}, \tag{1}$$

where j the complex conjugate and $\mathcal{H}\{x(t)\}$ is the Hilbert transform.

To obtain the envelope spectrum, the Fast Fourier Transform (FFT) is applied to the envelope signal $x_{\mathrm{a}}(t)$. The FFT significantly reduces the computational cost compared with the original Discrete Fourier Transform (DFT), lowering the complexity from N^2 to $N\log_2 N$ (Cooley and Tukey, 1965). The Discrete Fourier Transform (DFT) formula is explained as:

$$X[k] = \sum_{n=0}^{N-1} x[n] \cdot e^{-j\frac{2\pi}{N}kn}, \quad k = 0, 1, 2, \ldots, N-1 \tag{2}$$

where $\mathbf{X}[\mathbf{k}]$ is the output in the frequency domain, representing the complex value of the k-th frequency component; $\mathbf{x}[\mathbf{n}]$ is the input in the time domain, representing the value at the n-th time point; $\mathbf{N}$ is the total number of samples, representing the number of points in one period. $\mathbf{k}$ is the frequency index, ranging from $0, 1, 2, \ldots, N-1$, corresponding to different frequencies. $\mathbf{n}$ is the time index, ranging from $0, 1, 2, \ldots, N-1$, representing discrete time points. $\mathbf{j}$ is the imaginary unit, satisfying $j^2 = -1$.

The resulting envelope spectrum provides clear signatures of the characteristic bearing defect frequencies for a rotating inner ring: ball pass frequency outer race (BPFO), ball pass frequency inner race (BPFI), fundamental train frequency (FTF), cage frequency), ball spin frequency (BSF), and their harmonics (McFadden and Smith, 1984). These theoretical frequencies calculate as per:

$$\mathrm{BPFO} = \frac{z}{2} \cdot f_{\mathrm{r}} \cdot \left(1 - \frac{D_{\mathrm{W}}}{D_{\mathrm{pw}}} \cdot \cos\alpha\right) \tag{3}$$

$$\mathrm{BPFI} = \frac{z}{2} \cdot f_{\mathrm{r}} \cdot \left(1 + \frac{D_{\mathrm{W}}}{D_{\mathrm{pw}}} \cdot \cos\alpha\right) \tag{4}$$

$$\mathrm{FTF} = \frac{f_{\mathrm{r}}}{2} \cdot \left(1 - \frac{D_{\mathrm{W}}}{D_{\mathrm{pw}}} \cdot \cos\alpha\right) \tag{5}$$

$$\mathrm{BSF} = \frac{D_{\mathrm{pw}}}{D_{\mathrm{W}}} \cdot \frac{f_{\mathrm{r}}}{2} \cdot \left(1 - \left(\frac{D_{\mathrm{W}}}{D_{\mathrm{pw}}} \cdot \cos\alpha\right)^2\right) \tag{6}$$

where z is the number of rolling elements; $f_{\mathrm{r}} = \frac{\omega}{2\pi}$ is the rotational frequency of the shaft and ω is the rotation speed (rad/s); D_{W} is the diameter of the rolling element; D_{pw} is the pitch diameter of the bearing; α is the contact angle between the applied load and the radial plane of the bearing, which is $90°$ for a thrust bearing.

https://doi.org/10.5194/wes-2026-81
Preprint. Discussion started: 8 May 2026

eawe european academy of wind energy
Open Access WIND ENERGY SCIENCE DISCUSSIONS

In addition, a ring pass frequency on rolling element (RPBF) is considered in this work, defined as:

$$\mathrm{RPBF} = 2\,\mathrm{BSF}, \tag{7}$$

reflecting the fact that each roller damage excites both raceways per spin revolution in the tested thrust-bearing configuration.

Table 4 lists the calculated frequencies for a rotational speed of $\omega = 250rpm \cdot \frac{2\pi}{60sec/min} = 26.4rad/s$. Since the contact angle $\alpha = 0$ the ball pass frequency is the same for the outer and inner raceway.

Table 4. Characteristic frequencies of 81212 bearings in test at $\omega = 250rpm$, calculated with an approximate value for $D_{\mathrm{pw}} = \frac{d_o + d_i}{2}$ of 77.5 mm.

Frequency	Value in Hz
f_{r}	4.167
FTF	2.08
BPFO, BPFI	39.58
BSF	14.67
RPBF	29.35

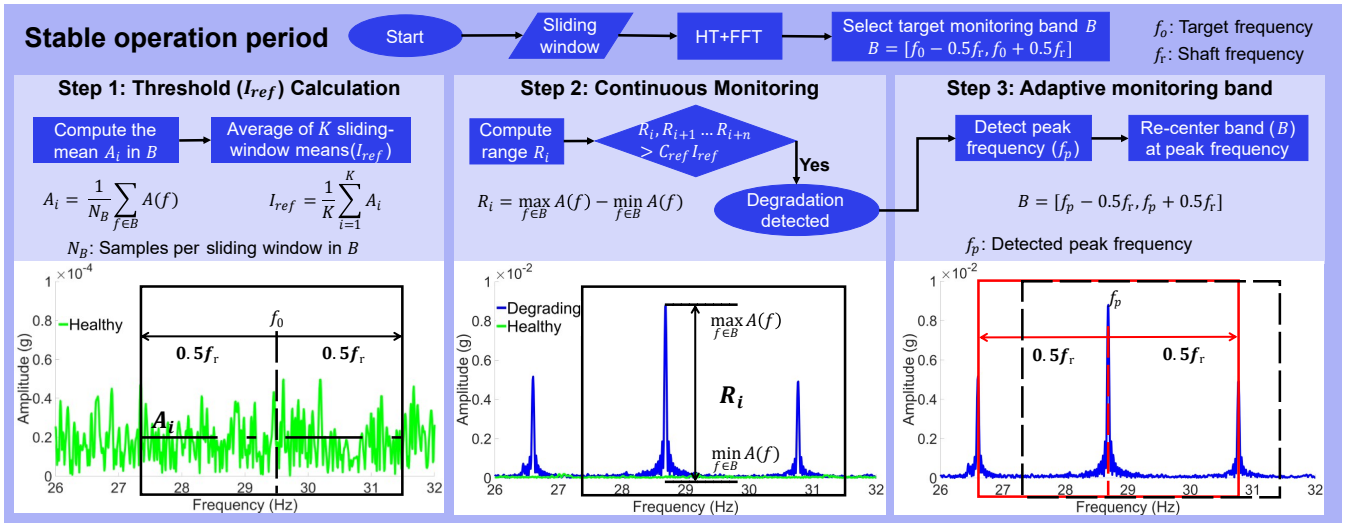

Figure 3. Flowchart of classical CM postprocessing as applied in this work; step 1: calculation of warning threshold; step 2: continuous monitoring of amplitude levels; step 3: adaptation of frequencies

In this work, abovementioned methods are applied as depicted in Figure 3. The vibration signal is processed in 30s-batches, and the amplitudes are evaluated for the characteristical frequencies. As damages to roller or raceways can influence the bearing kinematics and thus change these frequencies, each frequency is monitored in a frequency band. This band equals the monitored frequency plus and minus half the shaft frequency f_{r}.

https://doi.org/10.5194/wes-2026-81
Preprint. Discussion started: 8 May 2026

eawe european academy of wind energy
Open Access WIND ENERGY SCIENCE DISCUSSIONS

Step 1 describes the determination of normal behavior. For this, a period of stable operation after running-in is selected manually. For each frequency band, the average amplitude I_{ref} is calculated.

All subsequent data batches are then monitored for the maximum amplitude range R_i in step 2. If this value passes $10 \cdot I_{ref}$, a damage initiation is assumed. This threshold value is based on experience in operation and can differ for other monitored bearings and monitoring systems. Influencing factors are, i.e. the background noise of a complex machine or the sampling frequency of the data acquisition.

Step 3 involves an additional evaluation of the peak frequency in the frequency band to catch any events where frequency changes are larger than $0.5 \cdot f_{\mathrm{r}}$. For each data batch, the frequency with the highest peak is considered as the center frequency for the next batch. Note this step needs careful manual tuning in complex machinery with various characteristic frequencies in close proximity.

Other postprocessing techniques like bandpass filters were not applied in this work as all relevant frequency bands had a signal to noise ratio that allowed analyses without them. In more complex machines, they can allow earlier fault detection.

2.3 AI enhanced data processing

Deep learning models comprise numerous interconnected computational units organised in multiple layers, enabling them to learn non-linear data patterns through multiple levels of abstraction (LeCun et al., 2015). In this research, the AI-based high-level health indicator is derived from a normal behaviour multivariate autoencoder that fuses vibrational condition indicators. Autoencoders are trained to reproduce input data with a minimum reconstruction error (Rumelhart et al., 1986), and used for unsupervised learning tasks such as anomaly detection, feature extraction, and data generation (Berahmand et al., 2024). As

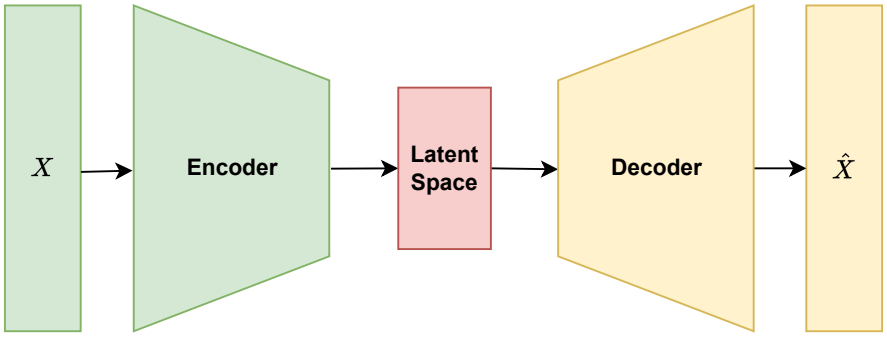

Figure 4. Overview of the autoencoder architecture, consisting of three main components: the encoder, latent space, and decoder. The model is trained to reconstruct an approximation $\hat{X}$ of the input X.

shown in Figure 4, the autoencoder consists of the encoder, latent space, and decoder. The encoder compresses the input into a lower-dimensional latent space, capturing the essential features required for reconstruction, while the decoder reconstructs the approximation of the input from the compressed representation.

https://doi.org/10.5194/wes-2026-81
Preprint. Discussion started: 8 May 2026

eawe european academy of wind energy
Open Access WIND ENERGY SCIENCE DISCUSSIONS

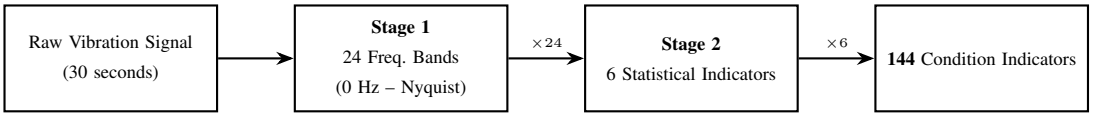

Figure 5. Overview of the signal processing pipeline to compute 144 condition indicators from the raw vibration signal.

The normal behaviour multivariate autoencoder is trained on condition indicators computed from vibration data measured during the healthy operation of the experimental bearing. The input condition indicators are calculated in two stages as depicted in Figure 5. In the first stage, frequency filtering following a binary-ternary tree is performed to enhance the frequency-based sensitivity of indicators (Antoni, 2007); 24 frequency bands from 0 Hz to the Nyquist frequency are computed from both the raw and preprocessed vibration signals. In the second stage, six statistical indicators, root mean square, crest factor, kurtosis, number of 4-sigma outliers, time negentropy, and spectral negentropy, are calculated for each frequency band obtained from the first stage (Peeters et al., 2019). Note that this is a non-exhaustive list of indicators and many more could be employed for signal characterization. The main consideration here is that the selected indicators should track at least in some way the level of non-stationarity and non-Gaussianity of the measured vibration signals (Antoni et al., 2024) as these characterize typical fault signatures. The selected healthy dataset D is a timeseries comprising M observations,

$$D = \{t_i | i = 1, ..., M\} \tag{8}$$

where each timestamp t_i contains a set of N condition indicators derived from vibration signal measurements of a sensor. Each timestamp t_i is represented as a vector X_i that contains N condition indicators, as defined in Equation 9.

$$X_i = \{x_1, x_2, x_3, ...x_N\} \tag{9}$$

The multivariate autoencoder is defined as a composite function consisting of an encoder f and a decoder g, trained jointly to optimise the encoder parameters ϕ and decoder parameters α.

$$\hat{X}_i = g_\alpha(f_\phi(X_i)) \tag{10}$$

The $\hat{X}_i$ is the approximation of the input X_i:

$$\hat{X}_i = \{\hat{x_1}, \hat{x_2}, \hat{x_3}, ...\hat{x_N}\} \tag{11}$$

The loss function $\mathcal{L}$ to calculate the reconstruction error between the input X_i and the reconstructed output $\hat{X}_i$ is defined as follows:

$$\mathcal{L} = \frac{1}{N}\sum_{j=1}^{N}(x_j - \hat{x}_j)^2 \tag{12}$$

N represents the number of condition indicators, x_j and $\hat{x}_j$ represent a single corresponding condition indicator value from the input Equation 9 and output Equation 11 vectors, respectively.

https://doi.org/10.5194/wes-2026-81
Preprint. Discussion started: 8 May 2026

eawe european academy of wind energy
Open Access WIND ENERGY SCIENCE DISCUSSIONS

The trained normal behaviour multivariate autoencoder on healthy condition indicators exhibits a bias towards reconstructing them with minimal error. As a result, the model struggles to reconstruct the condition indicator with faulty trends, which results in a higher reconstruction error. Therefore, the reconstruction error can be used as a high-level health indicator, representing the input condition indicators. The high-level health indicator represents a single point in the multidimensional condition indicators space.

Fault alarms are generated using the high-level health indicator, which is computed as a z-score value based on the reconstruction error between the model input and output. The z-score is a statistical measure that quantifies how many standard deviations a data point deviates from the mean of the learned normal behaviour. The z-score (z_i) is computed from the reconstruction error as defined in Equation 13.

$$z_i = \frac{\mathcal{L}_i - \mu}{\sigma} \tag{13}$$

The μ and σ represent the mean and standard deviation calculated from the reconstruction error of the healthy training dataset D after the completion of the training, as shown in Equation 14 and Equation 15.

$$\mu = \frac{1}{M}\sum_{i=1}^{M}\mathcal{L}_i \tag{14}$$

$$\sigma = \sqrt{\frac{1}{M}\sum_{i=1}^{M}(\mathcal{L}_i - \mu)^2} \tag{15}$$

The reconstruction error-based z-score consolidates the individual condition indicator's trends into a single high-level health indicator. During monitoring, the measured vibration signal is used to compute condition indicators, which are then input to the multivariate autoencoder to obtain the reconstruction error. The z-score, derived from the reconstruction error, quantifies the deviation of the current machine state from the learned normal behaviour. Fault notifications are generated by applying threshold levels to the high-level health indicator trend. Thresholds of 5 and 10 are used to classify the high-level health indicator into warning and alarm states, respectively. The threshold levels correspond to 5 and 10 standard deviations from the learned healthy behaviour of the machine, and the number of threshold levels and their values can be adjusted depending on the application requirements. High-level health indicator values below 5 are labelled as healthy, values between 5 and 10 indicate a warning state, and values exceeding 10 are classified as an alarm state. During real-time monitoring of the experimental setup, the high-level health indicator trend is continuously observed, and experts are notified when the trend exceeds the warning or alarm threshold levels.

3 Results

Table 5 gives an overview of the test results of this work. A total of five tests with ten tested bearings comprises the delivered data for condition monitoring. The total test time was approximately 129 days. In all cases, the rollers got damaged. After two

https://doi.org/10.5194/wes-2026-81
Preprint. Discussion started: 8 May 2026

of the five tests, the raceways also showed damages. Tests T1, T2, and T4 were stopped when the full-bandwidth acceleration of the test rig monitoring showed 1 g above stable operation values. Tests T3 and T5 were stopped upon crossing the threshold of the high-level indicator. Note the monitoring system did not have direct control of the test rig and the stopping was done manually after evaluation of the high-level indicator signal by a test engineer. T3 and T5 were stopped before the built-in limit of the test rig was triggered.

Table 5. Overview of bearing test results with test ID, durations, and observed damage.

Test ID	Test duration [h]	Damage on Bearing 1	Damage on Bearing 2	Data collection method	Test termination method
T1	825.9	No visible damage	One roller with spalling; raceways undamaged	Simcenter	Full-bandwidth 1 g limit
T2	289.6	Long spall mark on one raceway; spalling on multiple rollers	No visible damage	Simcenter	Full-bandwidth 1 g limit
T3	980.1	No visible damage	Small damage marks on one roller	Simcenter	AI-assisted test termination
T4	143	Extensive damage on multiple rollers and spalling mark on one raceway	No visible damage	Custom	Full-bandwidth 1 g limit
T5	849	No visible damage	Damage marks along the length of one roller	Custom	AI-assisted test termination

Figure 6 shows the results of test T1 after 825.9 h or 34.4 days. This test resulted in the damage of an individual roller of bearing 2. The left part of the figure shows the curves of the classical condition monitoring of RPBF in the top graph and the high-level indicator of the AI enhanced monitoring in the lower graph. The classical condition monitoring shows the Hilbert and Fast Fourier transformations for the ring pass on rolling element frequency band. The high-level indicator includes all frequency bands within the monitoring range and is not limited to one frequency. The accelerometer measures signals in three directions, x, y and z. z is the axial direction in which the load is applied. x is a radial direction. The dashed vertical lines indicate the first crossing of the fault threshold. For T1, the AI indicator crossed this threshold before the classical CM indicator.

The right part of the picture shows the rollers and the cage at the top and one of the raceways at the bottom. One of the rollers showed significant damages. The raceway shows some marks, which appear to be the consequences of particle overrollings and indicates an uneven load distribution with a clearly distinguishable discoloured contact track on the left part of the raceway. Pictures of all bearings in the tests are part of the appendix A.

Figure 7 shows the results of test T2 after 289.6 h or 12 days. This test resulted in the damage of several rollers and raceway spalling of bearing 1. The layout and components of Figure 7 are the same as Figure 6. The high-level indicator of the z-

https://doi.org/10.5194/wes-2026-81
Preprint. Discussion started: 8 May 2026

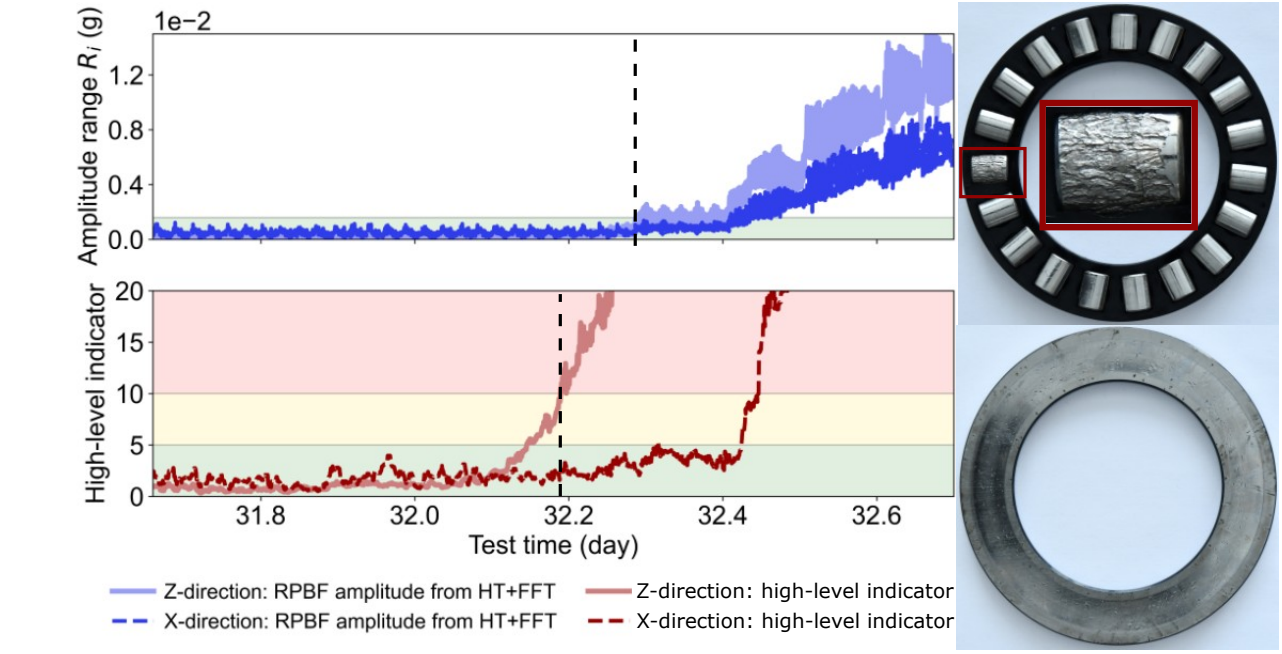

Figure 6. Results of test T1; left: condition monitoring output of classical and AI enhanced monitoring; right: bearing condition of bearing no. 2

direction triggered slightly before the static thresholds were passed. Note also the high-level indicator shows a significantly steeper incline than the HT+FFT values.

Figure 8, again with the same layout as the two previous figures, shows the results of test T3 after 980.1 h or 41 days. This test resulted in damages to one roller of bearing 2. In this case, the z-score passed the threshold slightly later than the HT+FFT postprocessing.

Figure 9, again with the same layout, shows the results of test T4 after 143 h or 6 days. This test resulted in the damage of several rollers and raceway spalling of bearing 1. In this case, the RPBF postprocessing did not pass the threshold at all, whereas the high-level indicator passed the threshold at approximately 4.5 days.

Figure 10, again with the same layout, shows the results of test T5 after 849 h or 35 days. This test resulted in the damage of one roller and raceway spalling of bearing 2. In this case, the RPBF postprocessing did not pass the threshold at all, whereas the high-level indicator passed the threshold at approximately 34.2 days.

Figure 11 depicts a waterfall plot of test T1. This plot shows frequencies from 1 to 50 Hz. The shaft frequency f_r is at 4.167 Hz and the $RPBF$ is at 29.35 Hz. A clear amplitude increase at $RPBF$ is observed closer to the end of the test and side-bands to $RPBF$ gradually appear at t = 32.4 days. This matches the changes observed in Figure 6, which contains only this frequency in the classical CM graph.

While Figure 11 basically confirms the information contained in Figure 6, the waterfall plots of tests T4 and T5, Figures 12 and 13, show different information. Figure 12 contains an additional amplitude increase at f_r, which is significantly higher

https://doi.org/10.5194/wes-2026-81
Preprint. Discussion started: 8 May 2026

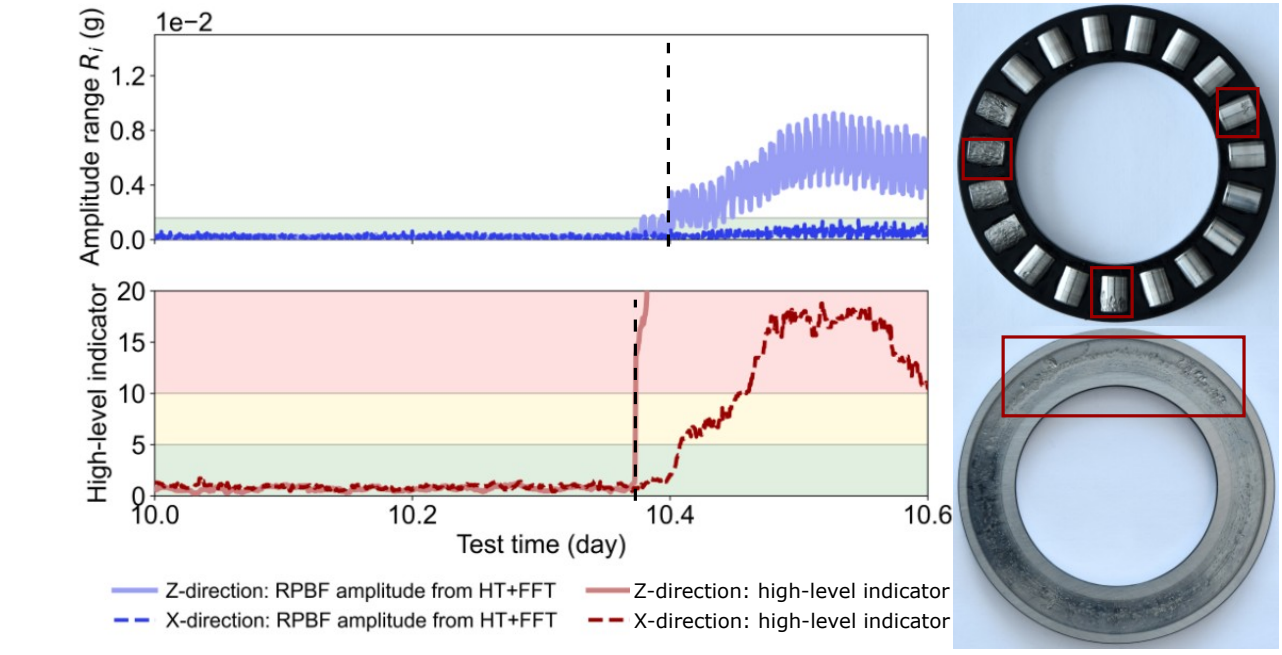

Figure 7. Results of test T2; left: condition monitoring output of classical and AI enhanced monitoring; right: bearing condition of bearing no. 1

than the increase at RPBF. Secondly the frequency of the RPBF peak is gradually moving towards lower frequencies during a period of almost one day. This can be explained by a lower rotation speed of a roller holding a damage region which is changing. Branching of the RPBF peaks might indicate damages of several rollers.

Figure 13 contains significant noise f_{r}, with several shorter periods of increased amplitudes.

4 Discussion and Conlusions

This work verifies potential benefits of using artifical intelligence in the postprocessing of condition monitoring data. Namely, it applies two approaches:

1. A multivariate autoencoder to train on normal behavior
2. A high-level indicator to summarize data from various sources

A small-scale bearing test rig conducted fatigue tests on axial roller bearings of type 81212. An accelerometer mounted to the rig and data acquisition units produced the data sets for the condition monitoring. The analyses results were used to answer the question if AI enhanced condition monitoring can perform similarly to classical condition monitoring.

The five conducted tests all resulted in damaged bearings. In three out of five tests, classical postprocessing and AI enhanced postprocessing passed warning thresholds close to each other. In the other two, the monitoring of the RPBF did not detect

https://doi.org/10.5194/wes-2026-81
Preprint. Discussion started: 8 May 2026

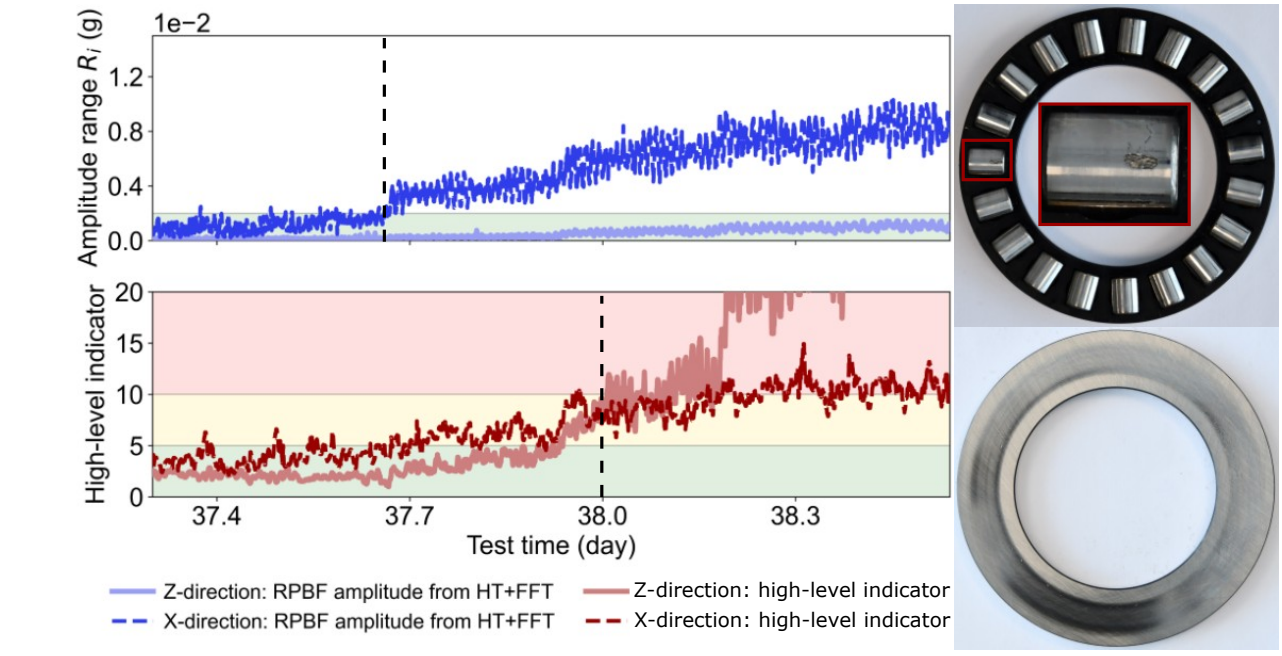

Figure 8. Results of test T3; left: condition monitoring output of classical and AI enhanced monitoring; right: bearing condition of bearing no. 2

damages, which the AI postprocessor detected. However, these damages resulted in higher amplitudes at shaft frequency and as classical condition monitoring commonly evaluates several frequencies, it is reasonable to assume that they were detected as well.

The AI postprocessor with a high-level indicator condenses the information of several frequency bands into one sensor-level graph which is easy to interpret. In more complex scenarios, this one graph does not only incorporate several frequency bands, but can also include several sources and sensors. This aggregation can be architected at various depths: from early fusion at the raw signal or feature level (multiple-input single output approaches), to late fusion where independent model decisions are voted upon (Hall and Llinas, 2002; Castanedo, 2013). Regardless of the stage at which this information is merged, the ultimate goal remains the same: to reduce high-dimensional monitoring data into a singular, actionable status for the machine.

In one case, a notable change in the frequencies was detected, most likely due to a change in bearing friction. The present work applied an automated approach to track such frequency changes by identifying the highest peak within a frequency band related to the kinematic frequency in question. Such an approach shows good results in a controlled environment with few excitation frequencies, but it needs considerable manual tuning in more complex or might even not succeed at all.

The results of this work are promising with regards to the application of AI enhanced postprocessing, particularly in more complex machines. In future works, similar approaches are going to be used on more complex test rigs with different bearing types in operation.

https://doi.org/10.5194/wes-2026-81
Preprint. Discussion started: 8 May 2026

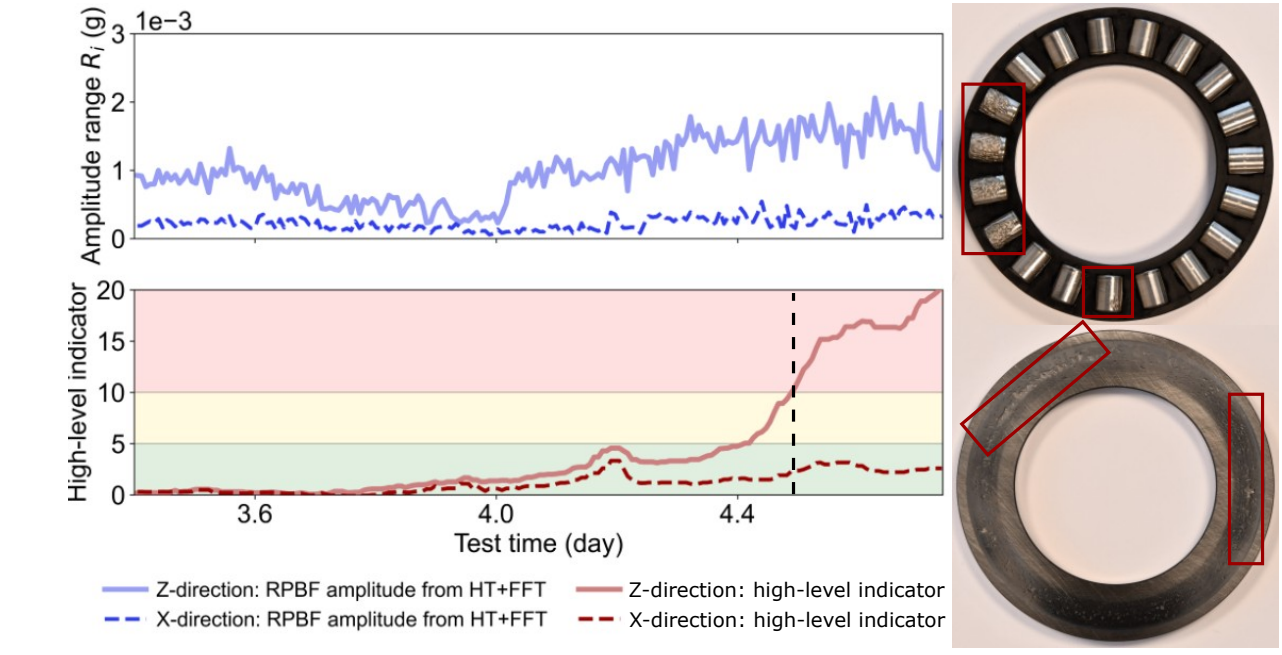

Figure 9. Results of test T4; left: condition monitoring output of classical and AI enhanced monitoring; right: bearing condition of bearing no. 1

Data availability. The raw vibration data is available via (Sudhakaran and Jamil, 2026)

Appendix A: Bearing component photographs

The bearings tested have been photographed after testing and are shown in Figures A1–A10.

Author contributions. Matthias Stammler: conceptualization, writing - original draft, review & editing
Faras Jamil: AI results, writing - original draft
Xinrun Liu: data analysis, classical CMS, result comparison, visualization, writing - original draft
Jens Jo Matthys: device preparation and data transfer, writing - original draft
Nikhil Sudhakaran: upgrading FE8 test rig, test execution, writing - original draft
Cédric Peeters: data post processing for AI CMS, writing - review & editing
Asger Bech Abrahamsen: upgrading FE8 test rig, writing - review & editing
Jan Helsen: writing - review & editing

Competing interests. All authors declare there are no competing interests

https://doi.org/10.5194/wes-2026-81
Preprint. Discussion started: 8 May 2026

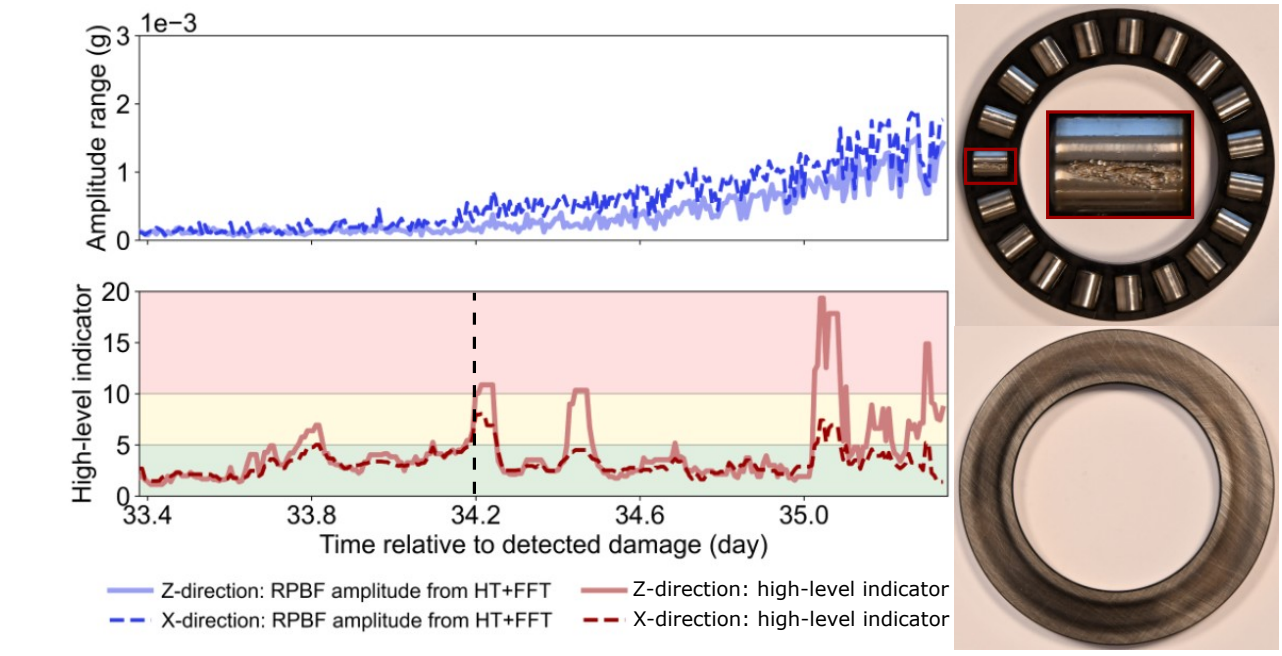

Figure 10. Results of test T5; left: condition monitoring output of classical and AI enhanced monitoring; right: bearing condition of bearing no. 2

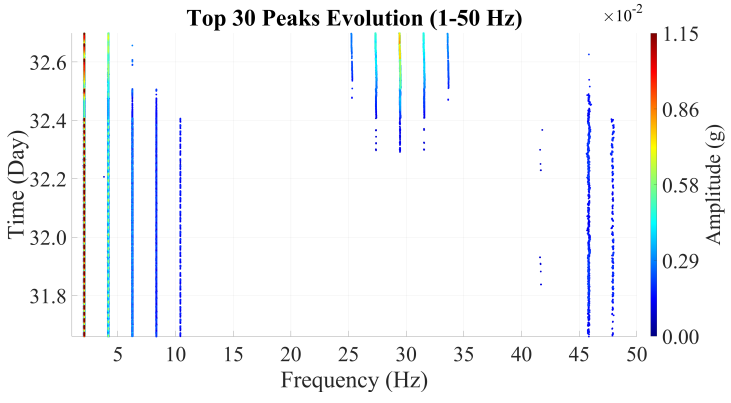

Figure 11. Results of test T1; waterfall plot across frequencies from 1 to 50 Hz in z-direction

Disclaimer. The authors disclaim this work to be a very good paper.

Acknowledgements. The authors would like to acknowledge FWO (Fonds Wetenschappelijk Onderzoek) for their support through the SB grants of Faras Jamil (#1S63123N), long stay abroad of Faras Jamil (#V405425N), and the EUDP funding of the DTU BOREAS (640241-521726) and MODA project (640242-534569).

https://doi.org/10.5194/wes-2026-81
Preprint. Discussion started: 8 May 2026

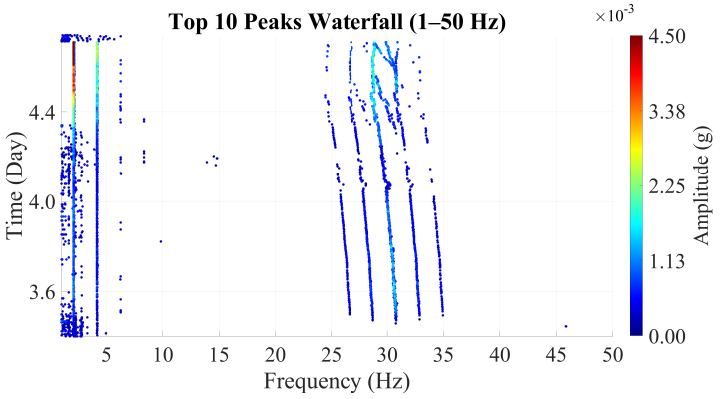

Figure 12. Results of test T4; waterfall plot across frequencies from 1 to 50 Hz in z-direction

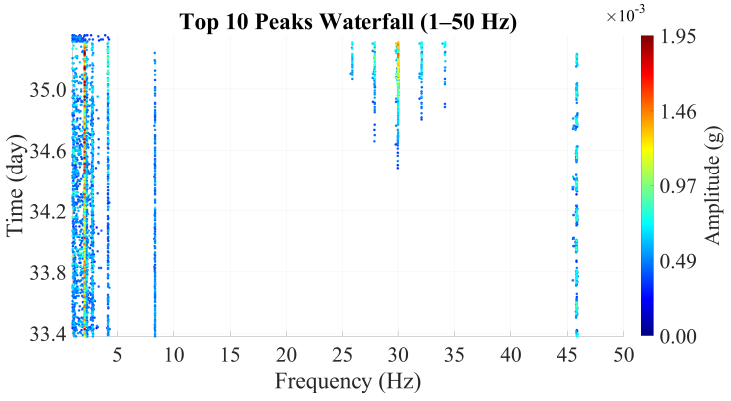

Figure 13. Results of test T5; waterfall plot across frequencies from 1 to 50 Hz in z-direction

References

Allen, J. B. and Rabiner, L. R.: Unified Approach to Short-time Fourier Analysis and Synthesis, Proc Ieee, 65, 1558–1564, 1977.

Antoni, J.: The spectral kurtosis: A useful tool for characterising non-stationary signals, Mechanical Systems and Signal Processing, 20, 282–307, https://doi.org/10.1016/j.ymssp.2004.09.001, 2006.

Antoni, J.: Fast computation of the kurtogram for the detection of transient faults, Mechanical Systems and Signal Processing, 21, 108–124, https://doi.org/10.1016/j.ymssp.2005.12.002, 2007.

Antoni, J., Kestel, K., Peeters, C., Leclère, Q., Girardin, F., Ooijevaar, T., and Helsen, J.: On the design of Optimal Health Indicators for early fault detection and their statistical thresholds, Mechanical Systems and Signal Processing, 218, 111 518, 2024.

Backwell, B., Clarke, E., Ladwa, R., Mullin, S., Jayasurya, F., Hutchinson, M., Qiao, L., Williams, R., Han, W., Liang, W., Fang, E., Francisco, A. M., Shardul, M., Gitobu, J., Cheong, J., Muchiri, W., Fiestas, R., Rabie, H., Madan, K., Weekes, N., Cargill, J., Lu, E., Sanchez, J. T., Melkonyan, N., Esteves, J., and Benoit, M.: GWEC Global Wind Report 2025, Tech. rep., GWEC, www.gwec.net, 2025.

https://doi.org/10.5194/wes-2026-81
Preprint. Discussion started: 8 May 2026

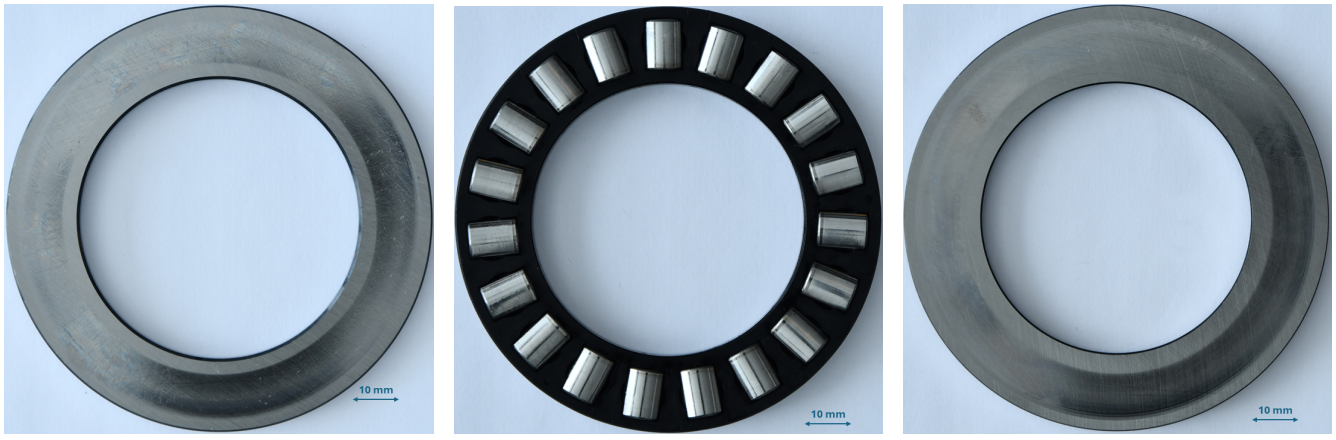

(a) Raceway 1 (b) Cage (c) Raceway 2

Figure A1. Pictures of bearing components for Bearing 1 of T01. Refer to Table 5 for designation of tests. The outer diameter of the bearing is 95 mm and the diameter and length of the rollers are both 11 mm.

(a) Raceway 1 (b) Cage (c) Raceway 2

Figure A2. Pictures of bearing components for Bearing 2 of T01. Refer to Table 5 for designation of tests. The outer diameter of the bearing is 95 mm and the diameter and length of the rollers are both 11 mm.

https://doi.org/10.5194/wes-2026-81
Preprint. Discussion started: 8 May 2026

(a) Raceway 1 (b) Cage (c) Raceway 2

Figure A3. Pictures of bearing components for Bearing 1 of T02. Refer to Table 5 for designation of tests. The outer diameter of the bearing is 95 mm and the diameter and length of the rollers are both 11 mm.

(a) Raceway 1 (b) Cage (c) Raceway 2

Figure A4. Pictures of bearing components for Bearing 2 of T02. Refer to Table 5 for designation of tests. The outer diameter of the bearing is 95 mm and the diameter and length of the rollers are both 11 mm.

https://doi.org/10.5194/wes-2026-81
Preprint. Discussion started: 8 May 2026

(a) Raceway 1 (b) Cage (c) Raceway 2

Figure A5. Pictures of bearing components for Bearing 1 of T03. Refer to Table 5 for designation of tests. The outer diameter of the bearing is 95 mm and the diameter and length of the rollers are both 11 mm.

(a) Raceway 1 (b) Cage (c) Raceway 2

Figure A6. Pictures of bearing components for Bearing 2 of T03. Refer to Table 5 for designation of tests. The outer diameter of the bearing is 95 mm and the diameter and length of the rollers are both 11 mm.

https://doi.org/10.5194/wes-2026-81
Preprint. Discussion started: 8 May 2026

(a) Raceway 1 (b) Cage (c) Raceway 2

Figure A7. Pictures of bearing components for Bearing 1 of T04. Refer to Table 5 for designation of tests. The outer diameter of the bearing is 95 mm and the diameter and length of the rollers are both 11 mm.

(a) Raceway 1 (b) Cage (c) Raceway 2

Figure A8. Pictures of bearing components for Bearing 2 of T04. Refer to Table 5 for designation of tests. The outer diameter of the bearing is 95 mm and the diameter and length of the rollers are both 11 mm.

https://doi.org/10.5194/wes-2026-81
Preprint. Discussion started: 8 May 2026

(a) Raceway 1 (b) Cage (c) Raceway 2

Figure A9. Pictures of bearing components for Bearing 1 of T05. Refer to Table 5 for designation of tests. The outer diameter of the bearing is 95 mm and the diameter and length of the rollers are both 11 mm.

(a) Raceway 1 (b) Cage (c) Raceway 2

Figure A10. Pictures of bearing components for Bearing 2 of T05. Refer to Table 5 for designation of tests. The outer diameter of the bearing is 95 mm and the diameter and length of the rollers are both 11 mm.

https://doi.org/10.5194/wes-2026-81
Preprint. Discussion started: 8 May 2026

Berahmand, K., Daneshfar, F., Salehi, E. S., Li, Y., and Xu, Y.: Autoencoders and their applications in machine learning: a survey, Artificial Intelligence Review, 57, 28, https://doi.org/10.1007/s10462-023-10662-6, 2024.

Burton, T., Jenkins, N., Sharpe, D., and Bossanyi, E.: Wind Energy Handbook, Wiley, ISBN 9780470699751, https://doi.org/10.1002/9781119992714, 2011.

Carroll, J., McDonald, A., and McMillan, D.: Failure rate, repair time and unscheduled O&M cost analysis of offshore wind turbines, Wind Energy, 19, 1107–1119, https://doi.org/10.1002/we.1887, 2016.

Castanedo, F.: A review of data fusion techniques, The scientific world journal, 2013, 704 504, 2013.

Chen, H., Liu, H., Chu, X., Liu, Q., and Xue, D.: Anomaly detection and critical SCADA parameters identification for wind turbines based on LSTM-AE neural network, Renewable Energy, 172, 829–840, https://doi.org/10.1016/j.renene.2021.03.078, 2021.

Chesterman, X., Verstraeten, T., Daems, P.-J., Nowé, A., and Helsen, J.: Condition monitoring of wind turbines and extraction of healthy training data using an ensemble of advanced statistical anomaly detection models, in: Annual Conference of the PHM Society, vol. 13, https://doi.org/10.36001/phmconf.2021.v13i1.2980, 2021.

Chesterman, X., Verstraeten, T., Daems, P.-J., Nowé, A., and Helsen, J.: Overview of normal behavior modeling approaches for SCADA-based wind turbine condition monitoring demonstrated on data from operational wind farms, Wind Energy Science, 8, 893–924, https://doi.org/10.5194/wes-8-893-2023, 2023.

Cooley, J. W. and Tukey, J. W.: An Algorithm for the Machine Calculation of Complex Fourier Series, Mathematics of Computation, 19, 297–301, https://doi.org/10.2307/2003354, 1965.

Du, W., Guo, Z., Li, C., Gong, X., and Pu, Z.: From Anomaly Detection to Novel Fault Discrimination for Wind Turbine Gearboxes With a Sparse Isolation Encoding Forest, IEEE Transactions on Instrumentation and Measurement, 71, 1–10, https://doi.org/10.1109/TIM.2022.3187737, 2022.

Gabor: Theory of communication, Journal of the Institution of Electrical Engineers, 93, 429–457, 1946.

Hall, D. L. and Llinas, J.: An introduction to multisensor data fusion, Proceedings of the IEEE, 85, 6–23, 2002.

Hart, E., Raby, K., Keller, J., Sheng, S., Long, H., Carroll, J., Brasseur, J., and Tough, F.: Main Bearing Replacement and Damage - A Field Data Study on 15 Gigawatts of Wind Energy Capacity, Tech. rep., NREL, https://doi.org/10.2172/1992019, 2023.

Haus, L., Sheng, S., and Pulikollu, R.: Newer/Larger Wind Turbine Reliability Analysis & Applications, in: Drivetrain Reliability Collaborative Workshop, 2025.

IEC: Wind turbines - Part 1: Design requirements, IEC 61400-1, International Electrotechnical Commission, Geneva, 4th edn., 2019.

ISO: Condition monitoring and diagnostics of machines — Vibration condition monitoring — Part 3: Guidelines for vibration diagnosis, ISO 13373-3, Geneva, Switzerland, 2015.

ISO: Condition monitoring and diagnostics of machines — Vibration condition monitoring — Part 2: Processing, analysis and presentation of vibration data, ISO 13373-2, Geneva, Switzerland, 2016.

ISO: Mechanical vibration - Measurement and evaluation of machine vibration: Part 21: Horizontal axis wind turbines, ISO 20816-21, Geneva, Switzerland, 2025.

Jamil, F., Verstraeten, T., Nowé, A., Peeters, C., and Helsen, J.: A deep boosted transfer learning method for wind turbine gearbox fault detection, Renewable Energy, 197, 331–341, https://doi.org/https://doi.org/10.1016/j.renene.2022.07.117, 2022.

Jamil, F., Jara Avila, F., Vratsinis, K., Peeters, C., and Helsen, J.: Wind turbine drivetrain fault detection using multi-variate deep learning combined with signal processing, in: Turbo Expo: Power for Land, Sea, and Air, vol. Volume 14: Wind Energy of *Turbo Expo: Power for Land, Sea, and Air*, p. V014T37A003, American Society of Mechanical Engineers, https://doi.org/10.1115/GT2023-101689, 2023a.

https://doi.org/10.5194/wes-2026-81
Preprint. Discussion started: 8 May 2026

Jamil, F., Peeters, C., Verstraeten, T., and Helsen, J.: Wind turbine drivetrain fault detection using physics-informed multivariate deep learning, in: Surveillance, Vibrations, Shock and Noise, Institut Supérieur de l'Aéronautique et de l'Espace [ISAE-SUPAERO], Toulouse, France, https://hal.science/hal-04166103, 2023b.

Jamil, F., Peeters, C., Verstraeten, T., and Helsen, J.: Leveraging signal processing and machine learning for automated fault detection in wind turbine drivetrains, Wind Energy Science, 10, 1963–1978, https://doi.org/10.5194/wes-10-1963-2025, 2025.

Kestel, K., Chesterman, X., Zappalá, D., Watson, S., Li, M., Hart, E., Carroll, J., Vidal, Y., Nejad, A. R., Sheng, S., Guo, Y., Stammler, M., Wirsing, F., Saleh, A., Gregarek, N., Baszenski, T., Decker, T., Knops, M., Jacobs, G., Lehmann, B., König, F., Pereira, I., Daems, P.-J., Peeters, C., and Helsen, J.: Condition monitoring of wind turbine drivetrains: State-of-the-art technologies, recent trends, and future outlook, Wind Energy Science Discussions, 2025, 1–85, https://doi.org/10.5194/wes-2025-168, 2025.

Khan, S. S. and Madden, M. G.: A Survey of Recent Trends in One Class Classification, in: Artificial Intelligence and Cognitive Science, edited by Coyle, L. and Freyne, J., pp. 188–197, Springer Berlin Heidelberg, Berlin, Heidelberg, ISBN 978-3-642-17080-5, https://doi.org/10.1007/978-3-642-17080-5_21, 2010.

Laouti, N., Sheibat-Othman, N., and Othman, S.: Support Vector Machines for Fault Detection in Wind Turbines, IFAC Proceedings Volumes, 44, 7067–7072, https://doi.org/10.3182/20110828-6-IT-1002.02560, 18th IFAC World Congress, 2011.

LeCun, Y., Bengio, Y., and Hinton, G.: Deep learning, Nature, 521, 436–444, https://doi.org/10.1038/nature14539, 2015.

McFadden, P. and Smith, J.: Model for the vibration produced by a single point-defect in a rolling element bearing, Journal of Sound and Vibration, 96, 69–82, https://doi.org/10.1016/0022-460X(84)90595-9, 1984.

Memija, A.: Dongfang Installs 'World's Largest Single-Capacity' Offshore Wind Turbine for Testing, https://www.offshorewind.biz/2025/09/03/dongfang-installs-worlds-largest-single-capacity-offshore-wind-turbine-for-testing/, 2025.

PCB: Model 356A03 | PCB Piezotronics, https://www.pcb.com/products?m=356a03.

Peeters, C., Verstraeten, T., Nowé, A., and Helsen, J.: Wind Turbine Planetary Gear Fault Identification Using Statistical Condition Indicators and Machine Learning, in: International Conference on Offshore Mechanics and Arctic Engineering, vol. Volume 10: Ocean Renewable Energy, American Society of Mechanical Engineers, https://doi.org/10.1115/OMAE2019-96713, 2019.

Poularikas, A. D., ed.: Handbook of Formulas and Tables for Signal Processing, CRC Press, Boca Raton, FL, 1st edn., https://doi.org/10.1201/9781315219707, 1998.

Pozo, F., Vidal, Y., and Salgado, : Wind Turbine Condition Monitoring Strategy through Multiway PCA and Multivariate Inference, Energies, 11, https://doi.org/10.3390/en11040749, 2018.

Randall, R. B. and Antoni, J.: Rolling element bearing diagnostics-A tutorial, Mechanical Systems and Signal Processing, 25, 485–520, https://doi.org/10.1016/j.ymssp.2010.07.017, 2011.

Rao, M., Yang, X., Chen, Y., Zuo, M., Bu, Z., Jin, Y., and Chu, F.: A new health indicator for rotating machinery condition monitoring under variable operation conditions through regression among vibration features, Mechanical Systems and Signal Processing, 241, 113 447, https://doi.org/10.1016/j.ymssp.2025.113447, 2025.

Rumelhart, D. E., Hinton, G. E., and Williams, R. J.: Learning internal representations by error propagation, Biometrika, 71, 6, https://doi.org/10.7551/mitpress/4943.003.0128, 1986.

Schaeffler: 81212-TV Axial cylindrical roller bearing, https://medias.schaeffler.dk/en/product/rotary/rolling-and-plain-bearings/roller-bearings/axial-cylindrical-roller-bearings/81212-tv/p/395947#Calculation, 2024.

https://doi.org/10.5194/wes-2026-81
Preprint. Discussion started: 8 May 2026

SKF: SKF Bearing Maintenance Handbook, SKF Group, ISBN 978-91-978966-4-1, https://cdn.skfmediahub.skf.com/api/public/0901d1968013be94/pdf_preview_medium/0901d196808383d3_pdf_preview_medium.pdf, pUB SR/P7 10001/1 EN, September 2011, 2011.

Sudhakaran, N. and Jamil, F.: Vibration Data from 81212 Bearing fatigue testing on FE8 Test Rig, https://doi.org/10.11583/DTU.31851214.v1, 2026.

Vestas: Vestas wins first order in Italy with a 35-year service agreement, https://www.vestas.com/en/media/company-news/2023/vestas-wins-first-order-in-italy-with-a-35-year-service-c3795806, 2023.

Zhao, H., Liu, H., Hu, W., and Yan, X.: Anomaly detection and fault analysis of wind turbine components based on deep learning network, Renewable Energy, 127, 825–834, https://doi.org/10.1016/j.renene.2018.05.024, 2018.